RESEARCH ARTICLE | SEPTEMBER 24 2024

Daytime thermal effects of solar photovoltaic systems: Field measurements

Daniel Trevor Cannon ⬤ ; Ahmad Vasel-Be-Hagh ✉ ⬤

Check for updates

View Online

Export Citation

Daytime thermal effects of solar photovoltaic systems: Field measurements

Daniel Trevor Cannon[1] (iD) and Ahmad Vasel-Be-Hagh[2,a)] (iD)

AFFILIATIONS

[1]Mechanical Engineering Department, Tennessee Tech University, Cookeville, Tennessee 38505, USA
[2]Mechanical Engineering Department, University of South Florida, Tampa, Florida 33549, USA

[a)]Author to whom correspondence should be addressed: vaselbehagh@usf.edu

ABSTRACT

Numerous gigawatt-scale solar installations will emerge globally within the coming decades, with the global solar installations growing to several hundred million acres by 2050. Understanding such extensive canopies' thermal and mechanical characteristics is crucial to developing an efficient site selection strategy and effective technologies to minimize and mitigate their potential environmental effects. This article shares the findings of a preliminary experimental study that aims to develop this understanding. This scaled, six-month-long field measurement campaign includes five photovoltaic panels instrumented by multiple heat flux, temperature, and humidity sensors, accompanied by wind anemometers and several pyranometers and pyrgeometers to measure incoming and outgoing shortwave and longwave radiations. In this article, the authors only compare fully sunny (no clouds) and completely overcast episodes. The research revealed that a quantitative comparison of upward radiation emitted and reflected by the surface of the panels and the ground using a scaled setup would not represent a utility-scale solar plant. This study also revealed the significant effect of the panels on surface heat flux, surface temperature, and air temperature. The panels also appeared to affect near-surface vertical turbulent heat and momentum fluxes. These effects intensify with increased incoming solar irradiance. Aside from providing a preliminary understanding of the effect of solar panels on surface and near-surface thermal characteristics, this study offers a valuable pool of data for validating computational models and feeding their boundary conditions. We will follow-up on this study by investigating a megawatt-scale solar farm using weather towers and full-scale computational simulations.

I. INTRODUCTION

Renewable energy's environmental and economic benefits are widely touted and recognized.[1] The ultimate goal of the energy science community is complete renewable-based electrification of all energy sectors by the mid-century.[2] In 2020, the global electricity generation was 25.9×10^{12} kW h, while the total world energy consumption was 169×10^{12} kW h.[3,4] In 2021, the world energy consumption was $\sim 177 \times 10^{12}$ kW h, with nearly 27.3×10^{12} kW h of it being electricity.[3,4] Comparing these two years indicates an almost 5% annual growth in energy consumption. This yearly growth rate suggests that a complete shift to renewable electrification by 2050 would require several hundred trillion kilowatt hour of renewable-based electricity. The atmosphere will source most of this electricity through wind and solar power. The neglected but crucial question is whether extracting such an enormous amount of energy from the atmospheric boundary layer (ABL) would alter the atmosphere's physics, leading to a new weather/climate change era for reasons other than criteria air pollutants. While mission-driven government agencies and industrial sectors focus entirely on extracting more energy from the atmosphere through wind or solar power, there is a dearth of scientific leadership and knowledge development to address this crucial question surrounding a complete renewable-based electrification of all sectors. For instance, the environmental clearances required for permitting photovoltaic (PV) plants (PVP) do not require assessing these plants' potential thermal impacts.[5]

Failing to address this concern on time could result in the same mistake the science and engineering communities made about fossil fuels. The obsession with inventing more powerful engines saturated these communities, so they overlooked the potential extent of the environmental impacts. Had such studies been conducted on the direct effects of fossil fuels on the atmosphere during the Industrial Revolution, the industrialization process could have been planned more efficiently, and the current pollution and climate change issues could have been avoided or, at least, be less severe.

Even in such an early stage of renewable-based electrification, utility-scale photovoltaic plants (PVP) create canopies that can spread across thousands of acres with millions of panels (e.g., Bhadla Solar Park of India with 10×10^6 panels spread over 14 000 acres, which is as large as one-fourth of the city of Boston[6]) and be as tall as 6.5 m (e.g., UPM 15X PV panel mounts[7]). In an article by the National Renewable Energy Laboratory (NREL), researchers predicted a global PV production of 10 TW by 2030 and 70 TW by 2050.[8] Almost six acres of installed PV panels are needed to produce 1 MW of electric power.[8] Hence, generating 70 TW of electricity via solar energy requires nearly 420×10^6 acres of PV installation by 2050, more extensive than four times the entire state of California. Given the gigantic scale of these developments, understanding and formulating PV-atmosphere interactions are socially, environmentally, meteorologically, and industrially crucial.

A few limited-scope numerical and experimental investigations have been conducted to evaluate the impact of PV plants on the near-ground temperature.[9–13] These studies are divided on their findings, with some reporting a reduction in the near-ground temperature[9,10] and some confirming a temperature increase.[11,12] Mixed theories have been proposed for either scenario.

The studies that report a reduction in the near-ground temperature argue that a PV plant converts more than 20% of the incoming solar power into electrical power. They hypothesize that the overall surface heat flux and near-ground temperature will decrease as the solar energy partially transmits away from the local environment in the form of electrical power.[9,10] Another argument supporting temperature reduction is that a PV installation introduces shading by light, thin material with a small total heat capacity (J/K), meaning it cannot store much incoming radiation. This shading would reduce the ground temperature and its upward heat flux.[9,10]

The studies confirming an increase in the near-ground temperature propose that PV panels' back surfaces block and return the upwelling longwave radiation, which can prevent the soil from cooling as much as it might under a dark sky at night. Burg *et al.*,[12] for instance, monitored air temperature at a PV plant, a nearby desert area, and a built environment for one continuous year and found that the average night temperature of the PV plant was ∼4 °C larger than the other two sites in spring and summer. The presence of the PV plant decreased the surface albedo by about 15%. Such a significant change in albedo would meaningfully alter the balance of absorption, storage, and release of short and longwave surface radiation.

These contradicting data and theories call for further systematic research. We have developed a five-year research program, including a two-stage field study and extensive computational fluid dynamics (CFD) simulations of different scales and resolutions, to address this gap and establish a comprehensive understanding of the interactions between PV plant canopies and the environment. The first phase of this study involved deploying a small-scale field study, including a setup of five panels, to gather relevant data. We concluded this small-scale measurement campaign in December 2023. This paper presents data and findings from this field investigation, focusing only on daytime data and comparing extreme cases of no cloud and overcast conditions. The article introduces the experiment's setup, the uncertainty and data quality control procedures employed, the theory applied to post-process the raw data, and an analysis of the observed trends. Unlike the previous studies presented in the literature, this study not only focuses on the air temperature but also measures and comments on surface temperature (ST), surface heat flux, longwave and short-wave radiation, wind speed, turbulence, vertical fluxes, and stability.

II. THE EXPERIMENTS

A. Timeline

This experimental setup collected data for six months, between June and December 2023, featuring both hot and cold seasons. This article, however, only focuses on presenting and comparing daytime data measured on episodes where there was either a complete overcast (hereafter referred to as *cloudy*) or no clouds observed in the sky (hereafter referred to as *sunny*). Partially cloudy, partially sunny, and nighttime data were not incorporated into the time averaging process. Such events will be shared in the future. The time-averaged data presented in this article were derived from ∼15 days characterized by cloudy conditions and 15 days characterized by sunny conditions.

B. The setup

Figure 1 demonstrates the overview of the experimental setup, featuring both an actual photograph and a detailed schematic. This experimental setup was on Tennessee Tech University's campus in Cookeville, TN (36°9′51″N 85°30′15″W).

The experimental configuration comprised five stationary 100 W photovoltaic panels arranged with a fixed tilt facing south. These panels charged a storage system supplying power to the data logger and all the instrumentation employed for data collection. This storage system utilized several batteries connected in parallel and an inverter to convert DC to AC.

Utilizing three sets of cameras, we observed the atmospheric conditions, the experimental arrangement, and the shadows cast by the panels onto the ground, all essential for data quality control and analysis. Monitoring the state of the sky allowed for distinguishing between days characterized by rainfall, fully and partially cloudy days, and those completely sunny. Observing the configuration using the second camera facilitated exploring potential factors behind anomalous trends in data, such as instances where avian interference impacted a specific sensor. Tracking the shading patterns of the panels via the third camera was essential to determine the period within which the sensors dedicated to measuring shading properties fell within the panel's shade.

The setup utilized a humidity sensor positioned 0.3 m above the unshaded ground to gauge relative humidity. It employed two ultrasonic anemometers, placed at 0.3 m height, to measure wind speed in the x-, y-, and z-directions: one positioned over the unshaded ground and the other above the shaded area. These measurements enabled the calculation of vertical heat and momentum fluxes within the air but very close to the surface (0.3 m above the ground).

The humidity sensor had an integrated thermocouple to record air temperature. The sonic anemometers also recorded air temperature by measuring the speed of sound and converting it to temperature, assuming a specific heat ratio of 1.4. Moreover, two air temperature sensors positioned above the panel surface at distances of 0.25 and 0.5 m recorded the air temperature atop the panels. The setup also incorporated four surface heat flux sensors with embedded thermocouples. These sensors were to determine heat flux and temperature on the front and back surfaces of the panel as well as on the shaded and unshaded ground surfaces.

24 September 2024 13:56:24
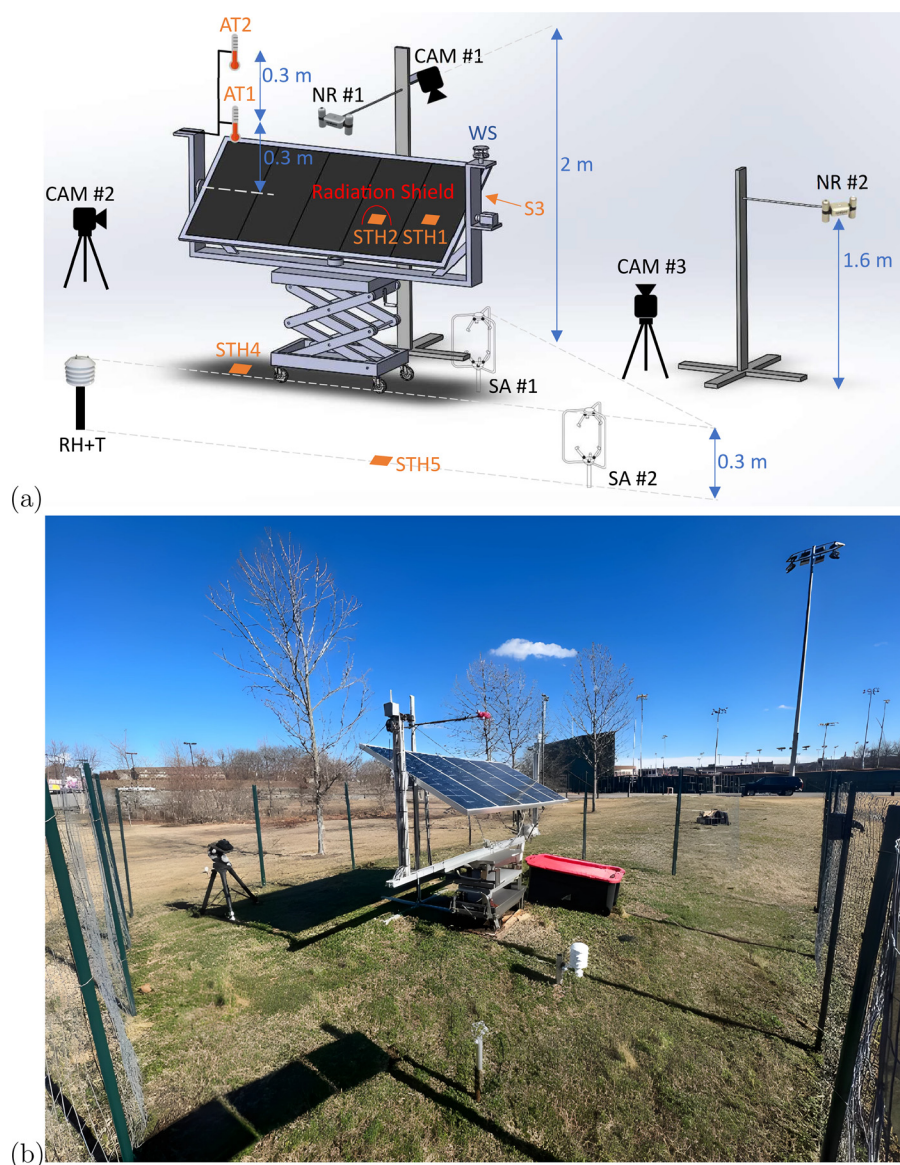
FIG. 1. (a) A schematic of the experimental setup. CAM: Camera; AT: Air Temperature Sensors; STH: Surface Temperature and Heat Flux Sensor; WS: Weather Station; RH+T: Humidity and Temperature Sensor; SA: Sonic Anemometer; NR: Net Radiometer. (b) The experimental setup in the field.

The experimental setup featured a pyranometer positioned within the plane of the solar panels, oriented toward the sky, to record shortwave radiation from 385 to 2105 nm received in the panel's plane. Additional data were collected using two net radiometers above the panels and the ground. Each net radiometer used a pair of pyranometers and pyrgeometers. One pyranometer/pyrgeometer pair faced upward to measure the total radiation from the sky. The other pair looked downward to probe the total radiation from the surface to the sky. The upward pyranometer measures radiation in the 385–2105 nm range, while the downward one captures radiation within the 370–2240 nm range. Note that the cutoff value of 2105 nm is appropriate because the irradiance beyond 2105 nm is a very small portion of the spectral irradiance at the earth's surface level after going through nearly 1.5 thickness of atmosphere (am 1.5 g).[14] In addition, for silicon,

i.e., the most popular type of PV panels, the spectral response extends between nearly 400 and 1200 nm (1.2 μm);[15] thus, the small portion of the spectral irradiance not being measured by the used pyranometer becomes even less significant. The pyrgeometer's spectral range was 5–30 μm. These sensors allowed for comparing the shortwave, the longwave, and the total net radiation above the ground vs the panels.

C. Data quality control

It was critical to process the large volumes of data collected daily throughout this research regularly to detect performance issues quickly. This research used Pecos, an open-source data quality control software developed by Sandia National Laboratory.[16–18] This Python-based script automatically allowed quality checks of an enormously

24 September 2024 13:56:24

large volume of time series data. All measurements of heat flux, temperature, relative humidity, radiation, and velocity were analyzed via Pecos to flag and remove problematic data points, leaving only good/clean data for calculating and presenting results. The quality checks included missing data, corrupt data, stagnant/unchanging data, abrupt changes in data, and data that fell out of a user-specified expected range.

More specifically, the entire set of measurements analyzed includes: (1) unshaded ground surface heat flux, (2) shaded ground surface heat flux, (3) front panel surface heat flux, (4) back panel surface heat flux, (5) unshaded ground surface temperature, (6) shaded ground surface temperature, (7) front panel surface temperature, (8) back panel surface temperature, (9) unshaded anemometer air temperature, (10) shaded anemometer air temperature, (11) air temperature 25 cm above the panel's front surface, (12) air temperature 50 cm above the panel's front surface, (13) air temperature at location of the relative humidity sensor (above the unshaded ground), (14) relative humidity above the unshaded ground, (15) downward/incoming shortwave radiation above the unshaded ground, (16) downward/incoming longwave radiation above the unshaded ground, (17) upward/outgoing shortwave radiation leaving the unshaded ground, (18) upward/outgoing longwave radiation leaving the unshaded ground, (19) downward/incoming shortwave radiation above the panel's front surface, (20) downward/incoming longwave radiation above the panel's front surface, (21) upward/outgoing shortwave radiation leaving the panel's front surface, (22) upward/outgoing longwave radiation above the panel's front surface, (23) x-component of air velocity of the unshaded anemometer, (24) y-component of air velocity of the unshaded anemometer, (25) z-component of air velocity of the unshaded anemometer, (26) x-component of air velocity of the shaded anemometer, (27) y-component of air velocity of the shaded anemometer, and (28) z-component of air velocity of the shaded anemometer.

Stagnant data were flagged and removed if the data remained constant throughout a 5 min moving window. Data blocks showing abrupt changes were flagged and removed if the data changed by an increment that was larger than a value specified by the user. These user-specified increments/values were carefully chosen depending on the measured data type (i.e., temperature, heat flux, etc.). For example, an abrupt change in air temperature of more than $4\,°C$ between two consecutive measurements is unreasonable. The user-specified cutoff increments for the 28 measurements previously mentioned are (1) $300\,W/m^2$, (2) $300\,W/m^2$, (3) $300\,W/m^2$, (4) $300\,W/m^2$, (5) $4\,°C$, (6) $4\,°C$, (7) $4\,°C$, (8) $4\,°C$, (9) $4\,°C$, (10) $4\,°C$, (11) $4\,°C$, (12) $4\,°C$, (13) $4\,°F$, (14) no incremental controls used for this measurement, (15) $900\,W/m^2$, (16) $100\,W/m^2$, (17) $900\,W/m^2$, (18) $100\,W/m^2$, (19) $900\,W/m^2$, (20) $100\,W/m^2$, (21) $900\,W/m^2$, (22) $100\,W/m^2$, (23) $10\,m/s$, (24) $10\,m/s$, (25) $10\,m/s$, (26) $10\,m/s$, (27) $10\,m/s$, and (28) $10\,m/s$. The final data quality control metric used was ensuring that the data points fell within the expected range. Similar to the abrupt data user-defined increments, we specified the expected data ranges for each measurement. For example, the incoming solar irradiation received at the edge of the earth's atmosphere remains relatively constant (referred to as the solar constant) and has a value of around $1300\,W/m^2$. As this solar radiation passes through the atmosphere, some of the radiation is absorbed and scattered, decreasing the total radiation received by the earth's surface. Additionally, the radiation value measured by the sensor should always be positive. Therefore, the expected range for data measured by

the radiation sensors should be between 0 and 1300 W/m^2. The user-specified ranges for all of the 28 measurements previously mentioned were (1) $(-700, 700)\,W/m^2$, (2) $(-700, 700)\,W/m^2$, (3) $(-700, 700)\,W/m^2$, (4) $(-700, 700)\,W/m^2$, (5) $(-18, 70)\,°C$, (6) $(-18, 70)\,°C$, (7) $(-18, 70)\,°C$, (8) $(-18, 70)\,°C$, (9) $(-18, 38)\,°C$, (10) $(-18, 38)\,°C$, (11) $(-18, 70)\,°C$, (12) $(-18, 70)\,°C$, (13) $(0, 140)\,°F$, (14) $(0, 100)\,\%RH$, (15) $(0, 1300)\,W/m^2$, (16) $(0, 1300)\,W/m^2$, (17) $(0, 1300)\,W/m^2$, (18) $(0, 1300)\,W/m^2$, (19) $(0, 1300)\,W/m^2$, (20) $(0, 1300)\,W/m^2$, (21) $(0, 1300)\,W/m^2$, (22) $(0, 1300)\,W/m^2$, (23) $(-10, 10)\,m/s$, (24) $(-10, 10)\,m/s$, (25) $(-10, 10)\,m/s$, (26) $(-10, 10)\,m/s$, (27) $(-10, 10)\,m/s$, and (28) $(-10, 10)\,m/s$.

D. Uncertainty analysis

Data measurement campaigns inherently include various sources of error. This study estimated the measurement error by superpositioning the calibration and resolution uncertainties to obtain a combined uncertainty, u_c, as

$$u_c = \sqrt{\sum u_i^2}, \qquad (1)$$

with i $= (1, 2)$ to represent calibration and resolution uncertainties, respectively. The calibration uncertainty is the variation between the recorded output of a properly calibrated instrument and the factual measurement of known target quantities. This difference can be caused by sensor drift, non-linearity in response, hysteresis effects, ambient noise, external interference, and environmental conditions. The sensor manufacturers provided the authors with the calibration uncertainties. According to the calibration sheets, the calibrations delivered by the manufacturers remain accurate for ∼12 months before necessitating sensor recalibration. Consequently, within this six-month measurement campaign, no interim recalibrations were deemed necessary. The resolution uncertainty is associated with the fineness to which the instrument can be read. The resolution of the digital sensors used in this research, such as the anemometers and the weather station, was specified by the manufacturers. The resolution of the analog sensors was determined by the 18 bit data logger and the voltage conversion coefficients provided by the sensor manufacturers. To achieve greater precision, we adjusted the voltage range of the data logger for each sensor, minimizing it as much as possible. This range could vary from as narrow as 30 mV to as wide as 100 V. To account for potential errors that might not be included in the calibration error, the total uncertainty, often called the expanded uncertainty, was estimated by multiplying the combined uncertainty u_c by a confidence factor $k > 1$. This research used $k = 1.5$; hence, uncertainties presented in this study are $U = 1.5 \times u_c$.

Table I presents the uncertainties associated with the sensors utilized in this investigation. Note that, in certain cases, the numerical value of the calibration depends on the measured value. Thus, as noted in the table, the combination of the calibration and resolution uncertainties found via Eq. (1) and, consequently, the expanded uncertainty shown in the total column is measurement-dependent in some cases. These uncertainties were transformed into error bars, visually represented on graphs within the Results and Discussion section (Sec. III).

This study required computing uncertainty of parameters that were functions of two or more variables, e.g., turbulent kinetic energy (TKE), defined as $TKE = (\overline{u'^2} + \overline{v'^2} + \overline{w'^2})/2$. Standard uncertainty propagation was applied in such instances.[19]

TABLE I. Instrument uncertainties. Most sensors (except the anemometers and the weather station) are analog; hence, their resolution is dictated by the 18 bit data logger's resolution. Repeatability and long-term drift uncertainties are included in the calibration uncertainties, except for the Apogee pyranometer, for which the repeatability is ~1%, and the long-term drift is ~2% per year.

Sensor	Measured parameter	Calibration	Resolution	Combined	Total
Hukseflux FHF04 (50 × 50 mm^2)	Panel's front and backsurface temperature	5%	1 C	Measurement dependent	Measurement dependent
	Panel's front and back surface heat flux	5%	0.025 W/m^2	Measurement dependent	Measurement dependent
Omega UHFS-09 (92 × 87 mm^2)	Shaded and unshaded ground's surface temperature	5%	1 C	Measurement dependent	Measurement dependent
	Shaded and unshaded ground's surface heat flux	5%	0.0016 W/m^2	Measurement dependent	Measurement dependent
Omega EWSA-PT1000	Air temperature above the panels	0.15 + 0.002T C	0.1 C	Measurement dependent	Measurement dependent
LI-560 TriSonica sphere wind flux sensor	Wind speed above unshaded ground	0.1 m/s	0.005 m/s	0.100 12	0.150 18
	Wind direction above unshaded ground	1°	0.5°	1.118 03	1.677 05
	Air temperature above unshaded ground	2 C	0.005 C	2.000 01	3.000 02
RM Young 8100 3D ultra-sonic anemometer	Wind speed above shaded ground	1% or 0.05 m/s	0.003	Measurement dependent	Measurement dependent
	Wind direction above shaded ground	3°	0.05°	2.000 62	3.000 94
	Air temperature above shaded ground	2 C	0.005 C	2.000 00	3.000 01
Apogee SL-510-SS and SL-610-SS Pyrgeometer	Long-wave radiation coming off or going into the sky	5%	0.008 W/m^2	Measurement dependent	Measurement dependent
Apogee SP-510-SS and SP-610-SS Pyranometer	Short-wave radiation coming off or going into the sky	5%	0.006 W/m^2	Measurement dependent	Measurement dependent
RM Yong 41382LF2 humidity/temperature	Air humidity above unshaded ground	1%	0.01 RH%	Measurement dependent	Measurement dependent
	Air temperature above unshaded ground	0.5 F	0.02 F	0.500 40	0.750 60
Tempest weather system	Wind speed above the panels	0.2 m/s	0.005 m/s	0.200 06	0.300 09
	Wind direction above the panels	3°	0.5°	3.041 38	4.562 07

E. Data processing

The measured data were processed into TKE, and the vertical momentum and heat fluxes. TKE was calculated using the fluctuating components of velocity in the x-, y-, and z-directions (u', v', and w') as

$$TKE = \frac{1}{2}\left(\overline{(u')^2} + \overline{(v')^2} + \overline{(w')^2}\right), \quad (2)$$

where $\overline{(u')^2}$ represents the time-averaged components of $(u')^2$ over a set interval.[20] Momentum and heat fluxes are calculated via

$$\tau = -\rho\overline{u'w'}, \quad (3)$$

and

$$H = \rho c_p \overline{w'\theta'}, \quad (4)$$

respectively, where ρ is the air density, c_p is the specific heat capacity, and θ is the potential temperature calculated as $\theta = T + (g/c_p)\Delta z$.

Suppose velocity components ($u_1 = 10$ m/s, $w_1 = 0.2$ m/s) and ($u_2 = 6$ m/s, $w_2 = 0.1$ m/s) were measured at times t_1 and t_2, respectively. Hence, $\overline{u} = (u_1 + u_2)/2 = 8$ m/s and $\overline{w} = (w_1 + w_2)/2 = 0.15$ m/s. This results in $u_1' = u_1 - \overline{u} = 10 - 8 = 2$ m/s. Similarly, $u_2' = -2$ m/s, $w_1' = 0.05$ m/s, and $w_2' = -0.05$ m/s. Therefore, $u_1'w_1' = (2)(0.05) = 0.1$ m^2/s^2 and $u_2'w_2' = (-2)(-0.05) = 0.1$ m^2/s^2, leading to $\overline{u'w'} = (0.1 + 0.1)/2 = 0.1$ m^2/s^2. For air, with $\rho = 1.2$ kg/m^3, vertical momentum flux is then $\tau = -\rho\overline{u'w'} = -(1.2$ kg/m$^3)(0.1$ m^2/s$^2) = -0.12$ N/m^2. This is how Eqs. (3) and (4) were applied to raw velocity and temperature data measured by the anemometers to obtain vertical momentum and heat fluxes.

III. RESULTS AND DISCUSSION

This six-month-long experimental study generated an extensive raw dataset, processed into thousands of figures and tables. While this article only presents a representative selection of these figures to exemplify the observed temporal variations, the values provided for

important parameters, such as air temperature difference atop panels and ground, are averaged across a total of 30 fully sunny (no cloud) and fully cloudy (overcast) days analyzed in this study.

A. Radiation

The setup comprised five pyranometers and four pyrgeometers. Among the pyranometers, two recorded shortwave radiation received by the panel in its plane and the vertical direction. The third measured the shortwave radiation received by the unshaded ground in the vertical direction. The remaining two pyranometers were meant to measure upward shortwave radiation reflected by both the panel and the unshaded ground in the vertical direction. As for the pyrgeometers, the upward ones measure incoming longwave radiation received by the panel and the unshaded ground in the vertical direction. The downward pyrgeometers were meant to record the emitted/reflected longwave radiation.

Installing a net radiometer too close to the surface would introduce errors since the readings would be too local and not representative of the surface. In addition, the sensor and its support structure would physically interfere with the measurements. Thus, the manufacturers recommend installing these sensors 1–2 m from the surface.[21] This is why we installed the net radiometer at 1.6 m. However, the net radiometer over the panel was installed at a closer distance of 0.5 m from the center of the panel. This was done mainly because the setup was small, and installing the sensor at a higher level would result in a very small view factor. Even this close distance led to a view factor of nearly 0.5; thus, the panel's net radiometer's measurements are not truly representative of a larger PV installation and are significantly affected by ground radiation. Hence, it was concluded that this scaled experimental setup does not allow for accurate measurement of radiative fluxes that are purely affected by the panels. Thus, this paper does not report upward shortwave and longwave radiations measured by the down-facing pyranometers and pyrgeometers.

Measuring the radiative components pursued two primary goals:

(1) We believe every other parameter of interest, such as the difference between the total heat flux at the shaded and unshaded ground, depends on the incoming radiation. We hypothesized that at least some of the panels' effects on the surface and near-surface thermal characteristics would become more significant as the incoming radiative fluxes increase. Thus, we measured all radiative components to investigate the correlation between the panel's impact on the near-ground properties and solar radiation.

(2) This study aimed to investigate the potential impact of installing PV panels on the canopy's absorbed or emitted radiation. The data collected throughout this campaign indicated that while the panel's presence narrowly increased upward and downward shortwave and longwave radiations, the change was insignificant as it fell within the margin of error of the measurements. This conclusion is not sound, primarily due to the low view factor of the net radiometer installed over the panels. In addition, these sensors do not perform well when simultaneously exposed to different emitting surfaces that radiate heat at different rates and in different directions, particularly when those surfaces are at different distances relative to the sensor—in this case, the panel surface and the ground surface farther away in the background fall in the sensor's field of view.

B. Camera data

The experiment involved a camera facing downwards to detect when a solar panel's shade covered the heat flux sensor and the anemometer designated to measure shaded conditions. All the cameras used in the experiment had a sampling frequency of 10 min. Figure 2 shows a sample recording taken by the camera on July 6, 2023, which includes a cloud event. This same analysis was conducted for every day. There are five essential elements in this figure: (1) the shaded anemometer, shown in Fig. 2(a), (2) the shaded heat flux sensor, also shown in Fig. 2(a), (3) the shade from the solar panel, (4) the shade from the trees [shown in Figs. 2(l) and 2(m)], and (5) the clouds passing atop the setup [shown in Fig. 2(h)]. As seen in Fig. 2, on July 6, 2023, the shade episode began at around 11:08. The anemometer and the heat flux sensor left the shade at almost 14:48 and 15:38, respectively. The anemometer remained shaded for about 3 h and 40 min. The heat flux sensor remained shaded for nearly 4 h and 30 min. We conducted the shaded vs unshaded ground analysis over these specific periods, which varied with the seasonal change in the Earth's tilt angle relative to the Sun. Thus, this shadow period assessment was performed for each day separately.

Three observations need to be highlighted. First, we did not include the first 10 min of shading periods in data processing because it would take some time for the sensors to respond to the shaded irradiance. Although it may not take 10 min for the sensors to respond, we had to use a 10 min buffer since the cameras were taking pictures every 10 min. Sampling at higher rates would create enormous data files, making it harder to maintain the experiment, including a need for switching the cameras' Secure Digital (SD) cards more frequently. Second, the start and end of the shading episodes varied depending on the season; thus, as mentioned before, we reevaluated these moments for each day. Third, the cloud events' timing differed from one day to another. Hence, the experiment also used a camera facing the sky to confirm these cloud episodes further [Fig. 1 (CAM #3)]. We excluded the cloud events when comparing shaded vs unshaded scenarios since all the sensors were shaded during the cloud events. Following the previously explained logic regarding the sensors' response time, we extended the filter by 10 min after each cloud event.

C. Heat flux

The experiment used four primary heat flux sensors (refer to Fig. 1) to measure the total heat flux, which included the sum of incoming and outgoing convective and radiative fluxes at the front and back surface of a panel as well as at the top of the shaded and unshaded ground surfaces. These sensors record a positive value if total heat flux enters the surface, i.e., heating the surface. They record a negative value if the total heat flux leaves the surface.

Figure 3 presents sample data measured by these sensors. The data shown in this figure belong to July 25, 2023. As previously explained in Sec. III B, the sensor designated to measure heat flux at the shaded ground is covered with the panel's shadow only for a few hours midday. Figure 3 includes a gray zone to denote this shadow period. In the depicted case (Fig. 3), the shadow period extended from 10:47 am to 03:47 pm. Figure 4 illustrates the heat flux sensor at the onset and conclusion of this specific shadow event. Note that the duration and
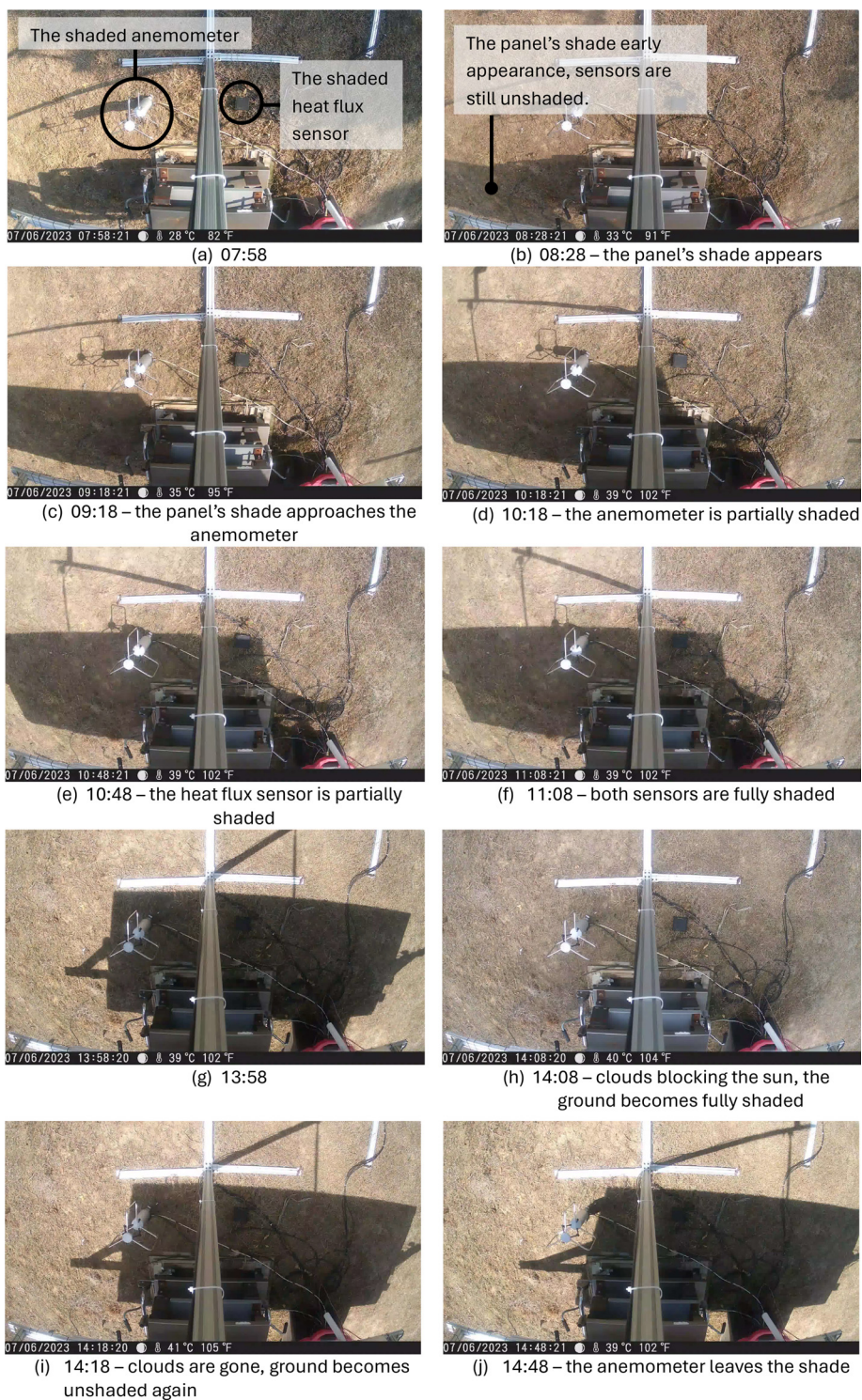
FIG. 2. Sample data recorded by the camera facing the ground on July 6, 2023. (a) 07:58, (b) 08:28—the panel's shade appears, (c) 09:18—the panel's shade approaches the Anemometer, (d) 10:18—the anemometer is partially shaded, (e) 10:48—the heat flux sensor is partially, (f) 11:08—both sensors are fully shaded, (g) 13:58; (h) 14:08—clouds blocking the Sun, the ground becomes fully shaded, (i) 14:18—clouds are gone, ground becomes unshaded again, (j) 14:48—the anemometer leaves the shade, (k) 15:38—the heat flux sensor leaves the shade, (l) 16:08—the shade of the adjacent trees enters the test area, and (m) 17:28—both sensors are covered by the trees shade.
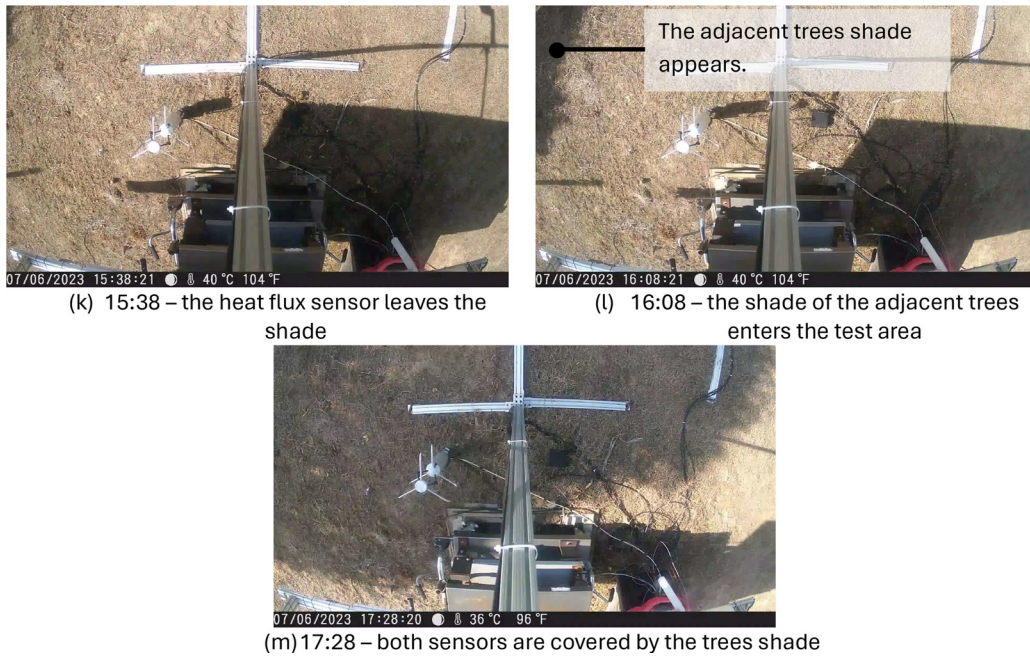
(k) 15:38 – the heat flux sensor leaves the shade

(l) 16:08 – the shade of the adjacent trees enters the test area

(m) 17:28 – both sensors are covered by the trees shade
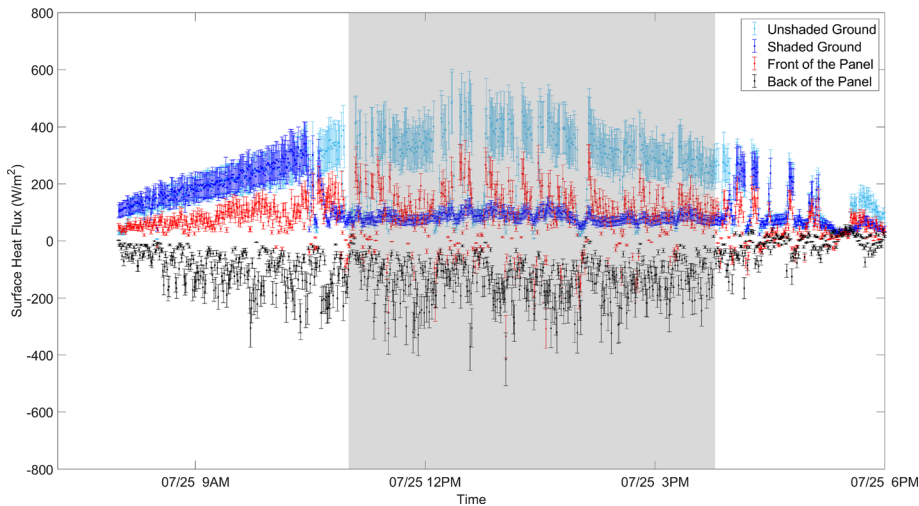
FIG. 2. (*Continued.*)

FIG. 3. Sample surface heat flux data recorded on July 25, 2023. The gray zone shows the shadow episode for the sensor designated to measure the shaded ground's heat flux.

FIG. 4. The shadow episode's beginning and end for the surface heat flux. The shadow enters the frame from the left and leaves from the right side. This shadow episode is shown as a gray window in Fig. 3.

timing of the shadow period vary with the seasons throughout this measurement campaign, from June to December 2023.

The sudden decrease in values measured by the ground's shaded heat flux sensor (shown in blue) is apparent once it enters the shade. The heat flux measured by this sensor starts rising immediately after the sensor leaves the shade. Such a trend would not be observed on a cloudy day. For instance, consider the data presented in Fig. 5 associated with August 2, 2023, a cloudy day at the experimental site. In Fig. 3, the subsequent fluctuations after the gray zone (after 15:47) are due to the partial shade of the adjacent trees [see Fig. 2(m)].

As mentioned, a positive heat flux signifies heat entering a surface, while a negative heat flux indicates heat exiting the surface. The only heat flux sensor that primarily measured negative values was attached to the back of the panels (Fig. 3, data shown in black). According to Fig. 3, the average heat flux at the unshaded ground was 275 W/m^2 on July 25, 2023. The average heat flux decreased to 84 W/m^2 when the panel's shadow shaded the ground, a nearly 70% reduction. Within this same time window, the overall heat flux at the panel's top surface was measured at 110 W/m^2, which is nearly 60% less than that absorbed by the unshaded ground.

We observed a consistent correlation between incoming solar radiation, especially shortwave radiation, and the disparity in heat flux between the panel and the ground surface. Incoming shortwave solar radiation averaged 351 W/m^2 over cloudy days. This value increased to 518 W/m^2 for sunny days. The change in incoming longwave radiation was less significant, varying from 496 on cloudy days to 539 W/m^2 on sunny days on average. We made two major observations.

First, the total heat flux at the unshaded ground was always larger than that at the panel's front surface by 73 (cloudy) and 175 W/m^2 (sunny), on average. This means the heat flux leaving the panel's front into the air is larger than that of the ground. This larger outgoing flux counteracts the incoming solar radiation, resulting in a reduced total heat flux at the panel's surface. One can attribute this observation to several factors:

(1) The panel has a considerably larger emissivity than the ground. Also, the panel's surface temperature is consistently higher than the ground's. It radiates more heat into the surroundings

compared to the ground. However, as explained in Sec. III A, the panels do not significantly impact the incoming and outgoing radiation components; thus, this factor cannot be a strong reason for the observed difference between the panel's and the unshaded ground's total heat flux.

(2) Since the panels are hotter than the ground, they convect more heat into the ambient. Similarly, this outgoing convection also partially offsets the incoming radiation.

(3) The convection heat transfer coefficient, h, is larger at the panel's surface, leading to larger outgoing convective fluxes. The larger h is due to two factors: (i) panels are installed higher than the ground; thus, they experience higher wind speeds, and (ii) panels are tilted, and the literature on heated flat plates is clear on the positive impact of tilt angle on the convection heat transfer coefficient.

(4) The panels have a very small capacity for storing heat relative to the ground, as is evident by the large heat flux leaving them through their back surface (an average of 131 W/m^2 on July 25, 2023).

Second, the panel's shade consistently decreased the total heat flux at the ground surface by an average of 44 (cloudy) and 186 W/m^2 (sunny). The smaller total heat flux into the shaded ground surface indicates that the shade caused by the PV installation decreases the heat stored in the ground, which can potentially result in two implications:

(1) We hypothesize that the ground would radiate less heat back into the sky during the night by decreasing the view factor between the ground surface and the space. One can draw an analogy between this effect and the nighttime impact of the contrails. Although only 25% of the flights occur at night, nighttime flights contribute to more than 60% of aviation's contrail effect on the climate because these clouds block the radiation of the heat into the sky, interfering with the cooling of the ground and the near-ground air. Thus, although less heat will be stored in the ground due to the panels' shade, the panels will prevent quick radiation of the stored heat into the sky at night, potentially leading to increased near-ground temperatures even at night.

(2) The heat that does not enter the ground due to the panel's shade would be "partially" advected to the surrounding environment,
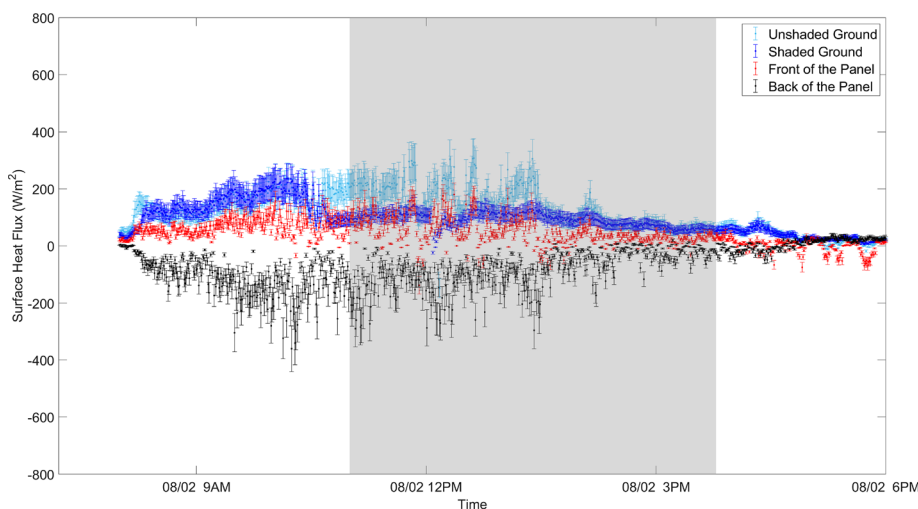

FIG. 5. Surface heat flux measured at a cloudy day (August 2, 2023). One can clearly tell the beginning of the long cloud episode before noon when heat fluxes at all different surfaces start converging.
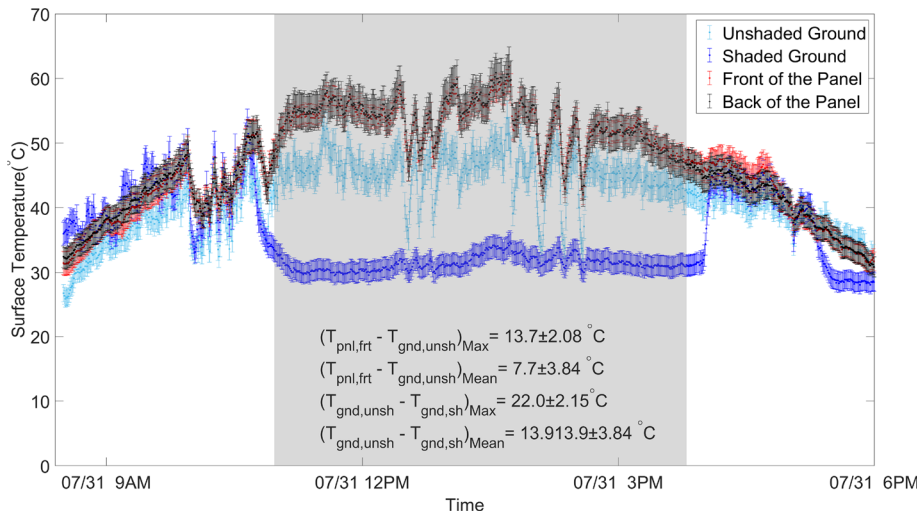
FIG. 6. Sample surface temperatures daily variation recorded on a sunny day (July 31, 2023).

resulting in increased daytime temperatures. This could be a reason for the increased air temperature above the panels discussed in Sec. III E. Note that parts of the blocked heat would convert to electricity via the cell. The split is currently unknown and, most likely, depends on many factors, such as the cell type. For instance, Cadmium Telluride cells absorb a significantly small fraction of short infrared up to only about 850 nm,[22] thus leaving more of the blocked heat advected into the surroundings. Silicon cells, however, can absorb shortwave infrared up to 1200 nm.

D. Surface temperature

This study evaluated surface temperatures on the ground (shaded and unshaded) and the panel (front and back). Figure 6 displays sample surface temperature data recorded on a sunny day (July 31, 2023). Comparisons should be confined to the gray window, indicating the period when the sensor designated to measure the shaded ground temperature was under the panel's shadow. Three key observations from Fig. 6 that held true on every sunny day include:

(1) The ground temperature significantly drops, particularly on sunny days, when covered by the panel's shade.
(2) The panel's temperature is significantly larger than the ground's.
(3) The panel's front and back surface temperatures were very close due to the panel being very thin with a very low heat storage capacity.

For the case shown in Fig. 6, the shaded ground was $13.6 \pm 3.8\,^\circ$C cooler than the unshaded ground on average. That day, this difference maximized at $22 \pm 2.1\,^\circ$C. The average difference between the panel's temperature and the unshaded ground was $7.7 \pm 3.8\,^\circ$C. This difference had a maximum of $13.7 \pm 2.0\,^\circ$C. These temperature differences showed a positive correlation with incoming solar radiation. To put this into perspective, Fig. 7 illustrates data collected on a cloudy day, indicating a much narrower gap between the panel, the shaded ground, and the unshaded ground temperatures. In this case, on average, the shaded ground was $4.6 \pm 3.6\,^\circ$C cooler than the unshaded ground. This difference peaked at $15.8 \pm 2.1\,^\circ$C that day. The average difference between
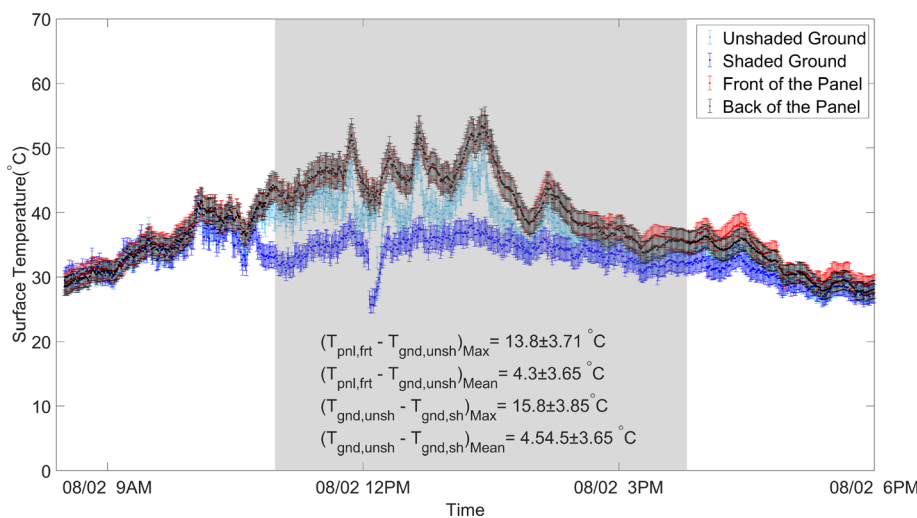

FIG. 7. Sample surface temperatures daily variation recorded on a cloudy day (August 2, 2023).

the panel's temperature and the unshaded ground was $4.3 \pm 3.6\,°C$. This difference had a maximum of $13.8 \pm 3.96\,°C$.

The temperature difference between the panel and unshaded ground surfaces averaged across all sunny days during this campaign was $6.7\,°C$. This corresponds to an average incoming shortwave radiation of $518\,W/m^2$ and an average incoming longwave radiation of $539\,W/m^2$. On the other hand, the average temperature difference on cloudy days was $3.9\,°C$. For cloudy days, the average incoming shortwave and longwave radiation was 351 and $496\,W/m^2$, respectively. The impact of the incoming solar radiation on the temperature difference between shaded and unshaded ground was even more significant. On sunny days, this difference averaged $11.1\,°C$, while it reduced to an average of $1.8\,°C$ on cloudy days.

The significance of the increased surface temperature is beyond its effect on the surrounding air temperature. While it may not be intuitive, this increased temperature can affect the entire mechanics of the atmosphere due to its role in atmospheric stability. When the canopy's surface is hot, the air near the ground is hotter than above, resulting in a decreasing vertical temperature profile. Consequently, disturbed air parcels moving upward encounter cooler, denser air, leading to buoyancy and further upward movement. This means the atmosphere is unstable because it amplifies disturbances. Therefore, a PV plant canopy resulting in an increased surface temperature during the day can lead to an even sharper decrease in temperature with elevation, creating more atmospheric instabilities.[23]

E. Air temperature

This study investigated how the PV panels affect the near-ground air temperature. The experiment measured the air temperature $\sim 30\,cm$ above both shaded and unshaded ground surfaces. Additionally, the air temperature was recorded at vertical distances of 25 and $50\,cm$ above the front surface of the panel. It is important to note that the panels were tilted, as with most PV panel installations, which means that the normal distances between the air temperature sensors and the panel's surface were actually less than the vertical distances given above. This explains the logic of measuring the air temperature $50\,cm$ above the panel (instead of $30\,cm$) to compensate for effects caused by the panel's tilt.

Figure 8 shares sampled air temperature variations recorded by these sensors. This figure presents data recorded on July 31, 2023. The average air temperature above the panel was nearly $9.4 \pm 0.62\,°C$ greater than the unshaded ground on that day. This temperature difference peaked at $12.3 \pm 0.88\,°C$. Similar to surface temperature and heat flux, the incoming irradiance also influenced the air temperature differences. Figure 9 shows the previously described air temperature variations on a cloudy day (August 3, 2023). It is evident from the figure that the air temperatures above the panel and the ground are much closer on a cloudy day with a much smaller incoming solar radiation. On average, the air temperature above the panel was larger by $\sim 4.4\,°C$ than the air temperature above the unshaded ground on cloudy days. However, this difference averaged $9.3\,°C$ on sunny days.

It is essential to explain why the air temperature above the panel is larger than the air temperature above the ground, while the total heat flux at the ground surface is larger than the total heat flux at the panel's top surface. As was explained in Sec. III C, the heat flux values measured by the surface heat flux sensors are total heat flux, including radiation and convection, with heat flux into the surface being positive and the heat flux leaving being negative. Thus, the lower total heat flux at the panel's top surface means more heat leaves that surface into the air than the ground's surface. This excess heat released into the air could be a primary reason for the air temperature increase. Under equal solar radiation rates, vegetated and semi-arid ecosystems release heat-dissipating latent energy fluxes via evapotranspiration, reducing sensible heat fluxes. In the presence of a PV plant canopy, latent fluxes decrease, leading to more significant sensible heat fluxes. This reduction in latent heat fluxes could also contribute to the increased air temperatures.[24,25]

This study also investigated the difference between the air temperature above the shaded vs unshaded ground. The average of these differences was $2.7\,°C$ over sunny days. This temperature difference averaged $1.7\,°C$ over all cloudy days studied herein. This observation prompts an inquiry. The temperature differential between the unshaded and shaded ground surfaces exceeded that between the unshaded ground and the panel's frontal surfaces. Therefore, the question arises: why is the temperature contrast between the air above the unshaded and shaded ground surfaces less than that above the unshaded ground and the panel's frontal surfaces? This arises from
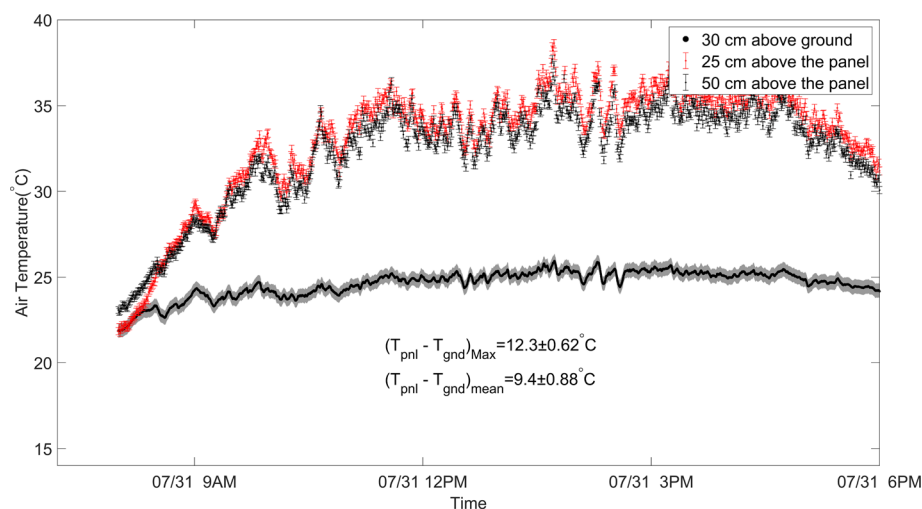

FIG. 8. Daily variations in air temperatures recorded on a sunny day (July 31, 2023).
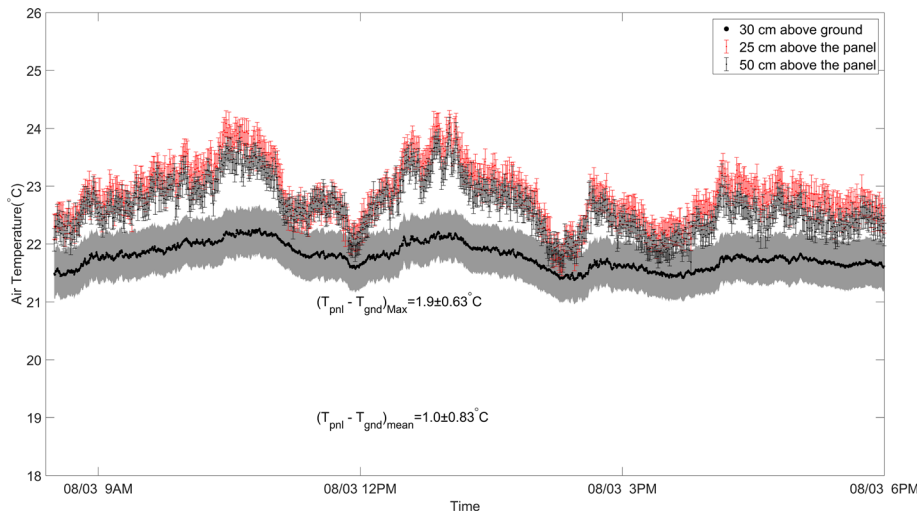
FIG. 9. Daily variations in air temperatures recorded on a cloudy day (August 03, 2023).

heat transfer through the panel, leading to increased air temperature directly beneath the panel where temperature measurements are taken above the shaded ground.

F. Wind speed, turbulence, and vertical fluxes

The experiment's scope also included understanding how the presence of the PV panels affects the near-ground wind speed, turbulence, and vertical fluxes. These questions were answered by analyzing the data collected via two ultrasonic anemometers, one in the panel's shade and one unshaded. The anemometers were mounted near the ground at a 30 cm height. By processing the wind speed components (u, v, and w) and temperature measured by these anemometers, one can obtain TKE, vertical momentum flux, and vertical heat flux [via Eqs. (2)–(4)] in the air atop the shaded and unshaded ground surfaces. Figure 10 shows the data recorded by the described anemometers for July 31, 2023. From the amplitude of the velocity components shown in the figure, it is clear that the panel impedes the velocity fluctuations, reducing turbulence. However, it does not decrease the mean wind speed, and occasionally, such as in the case shown in Fig. 10, the wind speed was even larger under the panel, i.e., above the shaded ground. This mean velocity increase is due to the decreased cross-sectional area of the flow passage. TKE decreased from 1.112 ± 0.31 to $0.377 \pm 0.1 \, \text{m}^2/\text{s}^2$ as the wind flew under the panel. Consequently, both vertical momentum and heat fluxes decreased significantly, from 0.407 to $0.014 \, \text{N/m}^2$ and 277.9 to $4.2 \, \text{W/m}^2$. The change in TKE, mean
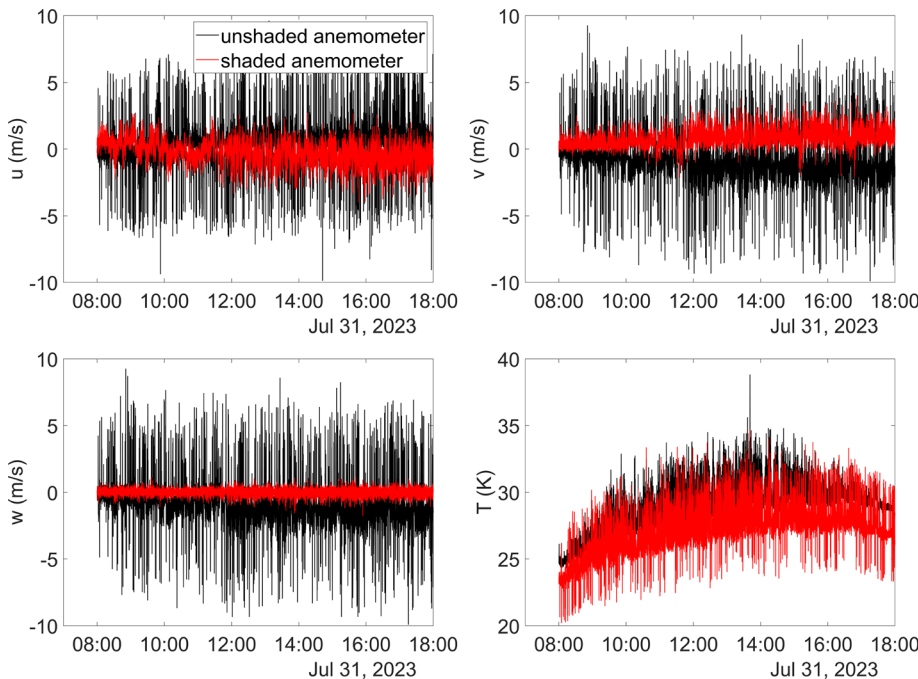

FIG. 10. Daily variations in wind speed components and temperature recorded by two anemometers above shaded and unshaded ground surfaces (July 31, 2023).

velocity, and vertical fluxes did not strongly correlate with solar irradiance. It seems these changes primarily stemmed from mechanical interference of the panel with the wind flow rather than their thermal effects.

Unfortunately, the setup did not include a third anemometer above the panel to examine TKE and vertical fluxes of momentum and heat at this location. This information is important and requires future investigations, either experimentally or numerically, via CFD.

IV. CONCLUSIONS

We performed a scaled field investigation to understand surface and near-surface thermal properties in the presence of PV panels. Covering bare soil or vegetated fields with millions of PV panels in utility-scale solar farms can change the surface properties by

(1) Altering surface reflectivity as the PV panels' reflectivity differs from that of soil or vegetated canopies.
(2) Making the overall surface color darker colorblue (e.g., grass versus grass partially covered by PV cells), altering its radiation emissivity and absorptivity.
(3) Increasing the convection heat transfer coefficient as the tall panels and their support structures are surface roughness elements that result in increased turbulence and vertical mixing.
(4) Providing physical coverage that slows the radiation of the heat stored in the air and the ground underneath the panels back to the sky.
(5) Converting energy to electricity and ships it away.
(6) Increasing sensible heat fluxes through the suppression of evapotranspiration. In the case of bare soil or vegetated canopies, evapotranspiration facilitates the release of heat-dissipating latent energy fluxes.

Under equal solar radiation rates, vegetated and semi-arid ecosystems release heat-dissipating latent energy fluxes via evapotranspiration. This reduces sensible heat fluxes and the amount of heat stored in the ground. In the presence of a PV plant canopy, however, latent fluxes decrease, leading to more significant sensible heat fluxes. The reduction in latent heat fluxes also leads to increased heat storage in the ground, eventually released back into the atmosphere after sunset.

These mechanisms have competing effects, with some promoting increased heating and some resulting in enhanced cooling. Thus, a field study was warranted to initiate the unraveling of the overall impact of these mechanisms and understand whether these mechanisms result in any significant alterations in the surface or near-surface thermal characteristics.

The observations presented in this article were drawn from daytime data collection. This study contrasts fully sunny and fully cloudy (overcast) days, excluding partially cloudy/sunny instances and nighttime data. Table II summarizes the data presented in this paper. The following is a highlight of the main observations from this investigation.

(1) The effect of PV panels on the surface and near-surface thermal characteristics increases with incoming solar irradiance, particularly with shortwave radiation. Thus, all the observations were more severe on sunny days compared to overcast days.
(2) The scaled setup was too small to accurately measure the net radiation above PV panels to compare them against those measured above the ground. Since we only had one row of five panels, the sensors above the panels also measured the radiation emitted/radiated from the surrounding ground surfaces. Thus, their measurements were not accurate.
(3) The total heat flux at the panel's top surface is less than the sunny ground. This observation indicates that a larger heat flux leaves the panel's surface into the air than the ground, offsetting the incoming solar irradiance.
(4) A panel's shadow significantly decreases the ground's total heat flux.
(5) The back and front surfaces of the panels are nearly at the same temperature. The panel's surface is significantly hotter than the ground's surface. The difference averages 6.7 and 3.9 °C on sunny and cloudy days, respectively.
(6) The air right above the panel is significantly hotter than above the sunny (unshaded) ground. The difference averages 9.3 and 4.4 °C on sunny and cloudy days, respectively.
(7) The average near-ground wind speed slightly increases under the panels. However, the turbulence and, consequently, vertical fluxes decrease as the wind flows under the panels.

It is important to note that this study was conducted at only one location, and that the results are expected to vary to some extent with changing the location, although the text of this variation remains to be explored. However, the value of such a study is

TABLE II. The time-averaged effect of PV panels on surface and near-surface thermal characteristics: fully sunny vs fully cloudy (overcast) days.

		Cloudy days	Sunny days
Time-averaged downward shortwave radiation		351 W/m^2	518 W/m^2
Time-averaged downward longwave radiation		496 W/m^2	539 W/m^2
		Time-averaged differences:	
Total surface heat flux (TSHF)	Larger on the sunny (unshaded) ground than the panel's front	73 W/m^2	175 W/m^2
	Larger on the sunny ground than the shaded ground (overcast via the panel)	44 W/m^2	193 W/m^2
Surface temperature (ST)	Larger at the panel's front than the sunny ground	3.9 °C (12%)	6.6 °C (15%)
	Larger the sunny ground than the shaded ground (overcast via the panel)	1.8 °C (6%)	11.1 °C (35%)
Air temperature	Larger atop the panel than the sunny ground	4.4 °C (20%)	9.3 °C (37%)
	Larger atop the sunny ground than the shaded ground	1.7 °C (8%)	2.7 °C (11%)

that it provides a precious resource for validating a CFD model that employs a solar calculator, such as the NREL's Solar Position and Intensity Code (Solpos), which requires global position (latitude, longitude, and time zone) as an input. The validated model can then be applied to other locations to investigate the effects discussed herein at various locations.

We are currently following up on the second stage of this research, which includes a measurement campaign at a utility-scale solar farm using 25 m tall meteorological towers. Upon their conclusion and analysis, the results of the large-scale field campaign accompanied by CFD simulations will be presented in the future. While the primary goal of our study at the utility-scale plant is to probe the solar plant's impact on the vertical profiles of temperature, wind speed, wind direction, and humidity, it will also reveal the extent to which the number of panels included in the study has an impact on the surface and near-surface properties, such as surface temperature or heat flux. Our research's ultimate goal is to parameterize solar farms and introduce them into weather models, such as Weather Research and Forecasting (WRF).

ACKNOWLEDGMENTS

AUTHOR DECLARATIONS
Conflict of Interest

The authors have no conflicts to disclose.

Author Contributions

Daniel Trevor Cannon: Conceptualization (equal); Data curation (equal); Formal analysis (equal); Investigation (equal); Methodology (equal); Software (equal); Writing – original draft (equal); Writing – review & editing (equal). **Ahmadreza Vasel-Be-Hagh:** Conceptualization (equal); Data curation (equal); Formal analysis (equal); Funding acquisition (equal); Investigation (equal); Methodology (equal); Project administration (equal); Resources (equal); Software (equal); Supervision (equal); Visualization (equal); Writing – original draft (equal); Writing – review & editing (equal).

DATA AVAILABILITY

The data that support the findings of this study are available from the corresponding author upon reasonable request.

REFERENCES

[1] I. Dincer and C. Acar, "A review on clean energy solutions for better sustainability," Int. J. Energy Res. **39**(5), 585–606 (2015).

[2] M. Z. Jacobson, M. A. Delucchi, Z. A. Bauer, S. C. Goodman, W. E. Chapman, M. A. Cameron, C. Bozonnat, L. Chobadi, H. A. Clonts, P. Enevoldsen, J. R. Erwin, S. N. Fobi, O. K. Goldstrom, E. M. Hennessy, J. Liu, J. Lo, C. B. Meyer, S. B. Morris, K. R. Moy, P. L. O'Neill, I. Petkov, S. Redfern, R. Schucker, M. A. Sontag, J. Wang, E. Weiner, and A. S. Yachanin, "100% clean and renewable wind, water, and sunlight all-sector energy roadmaps for 139 countries of the world," Joule **1**(1), 108–121 (2017).

[3] US Energy Information Administration, Primary energy (08/2023), see https://www.eia.gov/international/data/world/total-energy/total-energy-consumption.

[4] US Energy Information Administration, Electricity (08/2023), see https://www.eia.gov/international/data/world/electricity/electricity-generation.

[5] Office of National Environmental Policy Act Policy and Compliance, Eis-0448: Final environmental impact statement (08/2023), see https://www.energy.gov/nepa/articles/eis-0448-final-environmental-impact-statement.

[6] NS Energy, Bhadla solar park, Rajasthan (08/2023), see https://www.nsenergy-business.com/projects/bhadla-solar-park-rajasthan/.

[7] General Specialties Manufacturing, Inc., Mount sizing & pole specs (08/2023), see https://www.generalspecialtiesmfg.com/mount-sizing–pole-specs.html.

[8] S. Ong, C. Campbell, P. Denholm, R. Margolis, and G. Heath, "Land-use requirements for solar power plants in the united states," Technical Report No. NREL/TP-6A20-56290, National Renewable Energy Laboratory (NREL), Golden, CO, 2013.

[9] H. Taha, "The potential for air-temperature impact from large-scale deployment of solar photovoltaic arrays in urban areas," Sol. Energy **91**, 358–367 (2013).

[10] V. Masson, M. Bonhomme, J.-L. Salagnac, X. Briottet, and A. Lemonsu, "Solar panels reduce both global warming and urban heat island," Front. Environ. Sci. **2**, 14 (2014).

[11] G. A. Barron-Gafford, R. L. Minor, N. A. Allen, A. D. Cronin, A. E. Brooks, and M. A. Pavao-Zuckerman, "The photovoltaic heat island effect: Larger solar power plants increase local temperatures," Sci. Rep. **6**, 35070 (2016).

[12] B. R. Burg, P. Ruch, S. Paredes, and B. Michel, "Placement and efficiency effects on radiative forcing of solar installations," AIP Conf. Proc. **1679**, 090001 (2015).

[13] A. Vasel and F. Iakovidis, "The effect of wind direction on the performance of solar PV plants," Energy Convers. Manage. **153**, 455–461 (2017).

[14] A. J. Ali, L. Zhao, and M. H. Kapourchali, "Data-driven-based analysis and modeling for the impact of wildfire smoke on PV systems," IEEE Trans. Ind. Appl. **60**(2), 2076–2084 (2024).

[15] Z. Chen, Y. Zhong, Z. Ma, and M. Si, "Optimization design of surface optical characteristics of space solar cells based on transfer matrix method," Jpn. J. Appl. Phys., Part 1 **63**(3), 035501 (2024).

[16] S. Lindig, A. Louwen, D. Moser, and M. Topic, "Outdoor PV system monitoring—Input data quality, data imputation and filtering approaches," Energies **13**(19), 5099 (2020).

[17] W. F. Holmgren, C. W. Hansen, J. S. Stein, and M. A. Mikofski, "Review of open source tools for PV modeling," in *2018 IEEE 7th World Conference on Photovoltaic Energy Conversion (WCPEC) (A Joint Conference of 45th IEEE PVSC, 28th PVSEC & 34th EU PVSEC)* (IEEE, Waikoloa Village, HI, 2018), pp. 2557–2560.

[18] B. H. King, C. D. Robinson, C. Carmignani, D. Riley, and C. B. Jones, "Application of the Sandia array performance model to assess multiyear performance of fielded CIGS PV arrays," in *2018 IEEE 7th World Conference on Photovoltaic Energy Conversion (WCPEC) (A Joint Conference of 45th IEEE PVSC, 28th PVSEC & 34th EU PVSEC)* (IEEE, Waikoloa Village, HI, 2018), pp. 3607–3612.

[19] M. G. Morgan and M. Henrion, *The Propagation and Analysis of Uncertainty* (Cambridge University Press, 1990), pp. 172–219.

[20] J. C. Kaimal and J. J. Finnigan, *Atmospheric Boundary Layer Flows: Their Structure and Measurement* (Oxford University Press, 1994).

[21] Hukseflux Thermal Sensors, How to measure net radiation: A practical guide (08/2024), see https://www.hukseflux.com/library/how-to-measure-net-radiation-a-practical-guide.

[22] K. Chen, K. Hu, B. Zhao, T. Chen, Y. Hao, and G. Pei, "Spectral selectivity of CdTe cells with substrate configuration for photovoltaic/thermal applications," J. Therm. Sci. **33**(4), 1542–1553 (2024).

[23] C. Wang, H. Su, J. Zheng, S. Yu, L. Jiang, and H. Mo, "Strengthened impact of late autumn arctic sea ice on Asian winter cold extremes after 1999/2000," Environ. Res. Lett. **19**(7), 074045 (2024).

[24] C. S. Choi, J. Macknick, J. McCall, R. Bertel, and S. Ravi, "Multi-year analysis of physical interactions between solar PV arrays and underlying soil-plant complex in vegetated utility-scale systems," Appl. Energy **365**, 123227 (2024).

[25] T. M. Aschale, G. Sciuto, D. J. Peres, A. Gullotta, and A. Cancelliere, "Evaluation of reference evapotranspiration estimation methods for the assessment of hydrological impacts of photovoltaic power plants in Mediterranean climates," Water **14**(14), 2268 (2022).